Small influence of magnetic ordering on lattice dynamics in $TaFe_{1.25}Te_3$

M. Opačić,[1] N. Lazarević,[1] D. Tanasković,[2] M. M. Radonjić,[2] A. Milosavljević,[1] Yongchang Ma,[3,4] C. Petrovic,[3] and Z. V. Popović[1,5]

[1]*Center for Solid State Physics and New Materials, Institute of Physics Belgrade, University of Belgrade, Pregrevica 118, 11080 Belgrade, Serbia*

[2]*Scientific Computing Laboratory, Center for the Study of Complex Systems, Institute of Physics Belgrade, University of Belgrade, Pregrevica 118, 11080 Belgrade, Serbia*

[3]*Condensed Matter Physics and Materials Science Department, Brookhaven National Laboratory, Upton, New York 11973-5000, USA*

[4]*School of Materials Science and Engineering, Tianjin University of Technology, Tianjin 300384, People's Republic of China*

[5]*Serbian Academy of Sciences and Arts, Knez Mihailova 35, 11000 Belgrade, Serbia*

(Received 12 September 2017; published 16 November 2017)

Raman scattering spectra of zigzag spin chain $TaFe_{1.25}Te_3$ single crystal are presented in a temperature range from 80 to 300 K. Nine Raman active modes of A_g and B_g symmetry are clearly observed and assigned by probing different scattering channels, which is confirmed by lattice dynamics calculations. Temperature dependence of the Raman modes linewidth is mainly governed by the lattice anharmonicity. The only deviation from the conventional behavior is observed for A_g symmetry modes in a vicinity of the magnetic phase transition at $T_N \approx 200$ K. This implies that the electron-phonon interaction weakly changes with temperature and magnetic ordering, whereas small changes in the spectra near the critical temperature can be ascribed to spin fluctuations.

DOI: 10.1103/PhysRevB.96.174303

I. INTRODUCTION

The discovery of superconductivity in $La(O_{1-x}F_x)FeAs$ in 2008 [1] initiated an intensive search for new iron-based superconducting materials, in order to obtain better understanding of their physical properties and the mechanism of high-T_c superconductivity [2–4]. Novel iron-based materials, however, are not only superconducting, but can also exhibit various types of magnetic ordering. In some cases the magnetic phase transition is continuous [5–8], whereas in others it is accompanied by structural changes [9–15], or even by a nanoscale coexistence of antiferromagnetic (AFM) and superconducting domains [16–18].

$TaFe_{1+y}Te_3$ was synthesized and characterized about 25 years ago [19,20]. It is a layered system consisting of FeTe chains, along the b axis, separated by a Ta/Te network in between; see Fig. 1. These layers are parallel to the natural cleavage plane. There are also additional Fe ions, Fe2, randomly occupying interstitial sites [21–23]. $TaFe_{1+y}Te_3$ features anisotropic charge transport with metallic resistivity within the plane and insulating in the direction normal to the FeTe layers [23]. The first study of magnetic structure implies that $TaFe_{1+y}Te_3$ is composed of double zigzag spin chains with antiferromagnetic ordering of Fe1 spins [22]. The newest neutron diffraction measurements suggest that spin ordering within zigzag chains is ferromagnetic, whereas these zigzag chains couple antiferromagnetically [23], as shown in Fig. 1(b). However, the exact interaction mechanism is not clearly resolved.

There is a similarity between $TaFe_{1+y}Te_3$ and the extensively studied $Fe_{1+y}Te$ compound since they are correlated bad metals which order antiferromagnetically below $T_N \approx 200$ K and 70 K, respectively [10,23], both having rather large magnetic moments on Fe ions, $\approx 2\ \mu_B$/Fe. $TaFe_{1+y}Te_3$, however, forms ferromagnetic (FM) zigzag spin chains which couple antiferromagnetically between the layers, whereas the Fe spins in $Fe_{1+y}Te$ form a bicollinear AFM structure. The magnetic phase transition in $Fe_{1+y}Te$ is accompanied by the structural change from a tetragonal to a monoclinic, as opposed to $TaFe_{1+y}Te_3$ where a continuous transition to the AFM phase is observed in thermodynamic and transport measurements [22]. Just like in $Fe_{1+y}Te$, interest in spin chain and ladder materials [24] stems not only from their block-AFM states similar to parent compounds of iron-based superconductors [25], but also from superconductivity. It is worth noting that spin 1/2 copper oxide ladder structures host a spin gap and superconductivity upon doping [26–28]. In contrast to superconductivity in copper oxide ladder materials that was rather rare and with critical temperatures rather small when compared to highest achieved in copper square lattices [29,30], iron-ladder materials feature T_c's similar to the highest found in Fe-based superconductors [31].

Raman spectra provide additional information on magnetic ordering and electron-phonon coupling. There exist several Raman studies of the phonon spectra of iron based materials near the superconducting or magnetic phase transition [32,33]. While no anomalies were observed in 1111 compounds [34,35], the Raman spectra show anomalous behavior near the spin density wave (SDW) transition in some of the 122 and 11 compounds [15,36–38], which was ascribed to the phonon renormalization due to the opening of the SDW or superconducting gap, or to the structural transition. Large anomalies were observed also in ferromagnetic $K_xCo_{2-y}Se_2$ [5], which was ascribed to the effect of electron-phonon coupling and spin fluctuations. $Fe_{1+y}Te$ phonon spectra feature unusually large anomalies near the magnetic phase transition, as seen in sudden changes in the phonon frequencies and linewidths, due to the phonon modulation of magnetic interactions and structural phase transition [11–13]. Therefore, it is of interest to examine lattice dynamics in the normal state of iron-spin chain and ladder materials and compare it to materials like $Fe_{1+y}Te$. To the best of our knowledge, there are no published data on lattice dynamics of $TaFe_{1+y}Te_3$.

In this paper we present polarized Raman scattering spectra of $TaFe_{1.25}Te_3$ single crystal measured in a temperature range from 80 to 300 K. Nine out of 15 Raman active modes are

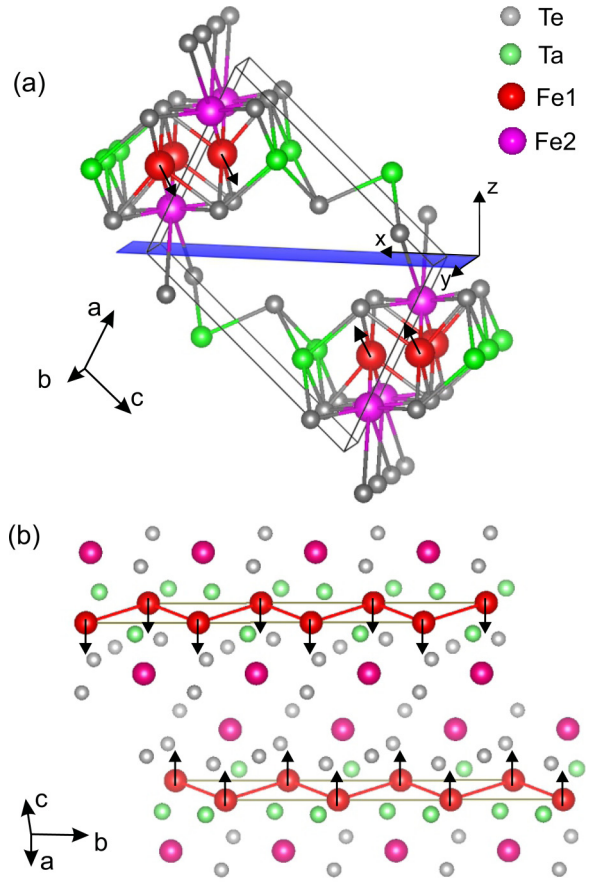

FIG. 1. (a) Structure of the $TaFe_{1.25}Te_3$ single crystal together with the natural cleavage plane $[\bar{1}01]$. $\mathbf{x} = 1/\sqrt{2}(\bar{1}0\bar{1})$ and $\mathbf{y} = (010)$ correspond to our laboratory system. (b) A view of the $TaFe_{1.25}Te_3$ structure along the b axis. Two neighboring chains of Fe1 spins point in a parallel direction, forming a ferromagnetic zigzag chain, whereas spins of neighboring zigzag chains order antiferromagnetically. One should note that Fe2 is present with occupancy of 0.25.

observed and assigned using the selection rules for different polarization configurations and lattice dynamics calculations. In a sharp contrast to the related FeTe compound, $TaFe_{1.25}Te_3$ Raman spectra do not show significant changes near $T_N \approx 200$ K, which clearly indicates that the phase transition is continuous. Temperature dependence of the frequency and linewidth is conventional, driven by the anharmonicity effects, except very near T_N where some of phonon lines slightly broaden which should be the consequence of spin fluctuations near the critical temperature. These results indicate very small changes in the electron-phonon coupling and in the Fermi surface in the measured temperature range.

II. EXPERIMENT AND NUMERICAL METHOD

Single crystals were grown using the self-flux method, as described elsewhere [19]. Raman scattering measurements were performed on freshly cleaved $(\bar{1}01)$-oriented samples, using Jobin Yvon T64000 Raman system, equipped with a nitrogen-cooled CCD detector, in the backscattering micro-Raman configuration. The 532 nm line of a solid state laser was used as an excitation source. A microscope objective with $50\times$ magnification was used for focusing the laser beam. All measurements were performed at low laser power, to reduce local heating of the sample. For low temperature measurements KONTI CryoVac continuous flow cryostat with 0.5 mm thick window was used. All spectra were corrected for the Bose factor. For extracting the data from the Raman spectra, phonon modes were fitted with a Lorentzian profile.

The electronic structure is calculated for stoichiometric $TaFeTe_3$ in the paramagnetic phase within the density functional theory (DFT), and the phonon frequencies at the Γ-point are obtained within the density functional perturbation theory (DFPT) [39], using the QUANTUM ESPRESSO package [40]. We have used projector augmented wave (PAW) pseudopotentials with Perdew-Burke-Ernzerhof (PBE) exchange-correlation functional with nonlinear core correction and Gaussian smearing of 0.01 Ry. The electron wave function and the density energy cutoffs were 64 Ry and 782 Ry, respectively. The Brillouin zone is sampled with $8 \times 8 \times 8$ Monkhorst-Pack k-space mesh. The phonon frequencies were calculated with the unit cell size taken from the experiments and the relaxed positions of atoms within the unit cell. The forces acting on individual atoms in the relaxed configuration were smaller than 10^{-4} Ry/a.u.

III. RESULTS AND DISCUSSION

$TaFe_{1+y}Te_3$ crystallizes in the monoclinic crystal structure, which is shown in Fig. 1. The space group is $P2_1/m$ (unique axis b), with two formula units per unit cell [19,20]. The experimental values of the unit cell parameters are $a = 7.436$ Å, $b = 3.638$ Å, $c = 10.008$ Å, and $\beta = 109.17^\circ$. All atoms (including the excess Fe), are at $2e$ Wyckoff positions, with fractional coordinates given in Table I.

The factor group analysis (FGA) for $P2_1/m$ space group yields the following normal mode distribution at the Γ point:

$$\Gamma_{\text{Raman}} = 10A_g + 5B_g,$$
$$\Gamma_{\text{IR}} = 4A_u + 8B_u,$$
$$\Gamma_{\text{acoustic}} = A_u + 2B_u.$$

The Raman spectra were measured from the $(\bar{1}01)$ plane of the sample, which is the natural cleavage plane [23,42]. From the Raman tensors given in Table II, the A_g phonon modes are expected to be observable in the (xx) and (yy) scattering configurations. The B_g modes can be observed only in (xy) polarization configuration.

TABLE I. Experimental fractional coordinates of $TaFe_{1.25}Te_3$ taken from Ref. [19]. In the parentheses are the calculated values for $TaFeTe_3$.

Atom type	x	y	z
Ta	0.8340 (0.8331)	0.25	0.3007 (0.2987)
Fe1	0.6147 (0.6223)	−0.25	0.0890 (0.0988)
Fe2	0.7686	0.25	−0.0047
Te1	0.4392 (0.4326)	0.25	0.1860 (0.1637)
Te2	0.9835 (0.9842)	−0.25	0.1589 (0.1584)
Te3	0.2179 (0.2192)	0.25	0.4970 (0.5028)

TABLE II. Upper panel: atomic species (all of them are at 2*e* Wyckoff positions) and the contribution of each atom to the Γ-point phonons, the corresponding Raman tensors for the $TaFeTe_3$ single crystal ($P2_1/m$ space group) [41]. Lower panel: the calculated (for the stoichiometric $TaFeTe_3$) and experimental phonon energies at 100 K (for the $TaFe_{1.25}Te_3$ single crystal).

Atoms	Irreducible representations
Ta, Fe1, Te1, Te2, Te3	$2A_g + A_u + B_g + 2B_u$

Raman tensors

$$\hat{R}_{A_g} = \begin{pmatrix} a & 0 & d \\ 0 & b & 0 \\ d & 0 & c \end{pmatrix} \qquad \hat{R}_{B_g} = \begin{pmatrix} 0 & e & 0 \\ e & 0 & f \\ 0 & f & 0 \end{pmatrix}$$

Raman active			Infrared active		
Symmetry	Calc. (cm^{-1})	Expt. (cm^{-1})	Symmetry	Calc. (cm^{-1})	Expt. (cm^{-1})
A_g^1	36.2		A_u^1	42.8	
B_g^1	43.8		B_u^1	54.9	
B_g^2	57.9	61.6	B_u^2	94.4	
A_g^2	63.8	62.3	A_u^2	101.4	
A_g^3	75.3	68.5	B_u^3	111.3	
A_g^4	104.4	90	A_u^3	131.1	
B_g^3	105.1		B_u^4	143.2	
A_g^5	124.6		B_u^5	160.4	
B_g^4	127.2	130.4	B_u^6	188.6	
A_g^6	149.8	155	B_u^7	227.9	
A_g^7	164.9	165	A_u^4	231.1	
A_g^8	191		B_u^8	289.4	
B_g^5	217.1	222.3			
A_g^9	241.9	223.9			
A_g^{10}	276.22				

Raman scattering spectra of $TaFe_{1.25}Te_3$ single crystals, measured at 100 K in three different polarization configurations, are presented in Fig. 2. By using the selection rules, we assign the Raman peaks appearing in the (xx) and (yy) polarization configuration as the A_g ones. This conclusion is supported by the lattice dynamics calculations, given in Table II. By comparing the calculated values of A_g mode energies with those of the peaks appearing in the (xx) and (yy) spectra, we can unambiguously assign four Raman modes (A_g^4, A_g^6, A_g^7, and A_g^9). The broad structure around 65 cm^{-1} probably originates from the A_g^2 and A_g^3 modes, although the contribution of the A_g^1 mode (with calculated energy of 42.7 cm^{-1}) cannot be excluded. The peaks at 57.9 cm^{-1} and 130 cm^{-1} that are clearly visible in (xy) but absent in (yy) configuration are assigned as B_g^2 and B_g^4 modes, respectively. The low intensity peak at ≈220 cm^{-1}, that becomes clearly observable at low temperatures, is tentatively assigned as B_g^5 mode, although the contribution from the leakage of A_g^9 mode cannot be excluded. The origin of the two very broad structures at about 70 cm^{-1} and 160 cm^{-1}, which are pronounced in the (xy) configuration, is not completely clear. Aside from providing additional charge, Fe2 atoms may contribute to momentum transfer scattering, in line with the pronounced quasielastic continuum, present in all the scattering configurations. Consequently, contribution from single-phonon scattering away from Γ point becomes observable, which is theoretically predicted [43,44] and experimentally observed [45,46]. Although we cannot exclude the possibility of two- and, in particular, double-phonon contributions, we believe it is less likely due to the nature of the processes and since they usually have more pronounced contribution to A channel (for arbitrary irreducible symmetry μ of C_{2h} holds $\mu \otimes \mu \ni A$).

The normal modes of the selected A_g and B_g vibrations, as obtained by the lattice dynamics calculations, are shown in Fig. 3. The low energy B_g^2 mode represents vibrations of Te and Ta atoms which tend to elongate the (Ta,Fe)Te tetrahedra in the xy plane. B_g^4 phonon originates mainly from Ta and Te atom vibrations in directions opposite to each other, whereas A_g^4 mode represents dominantly vibrations of another Te atom in the xy plane. A_g^7 and A_g^9 modes originate from the vibrations of Fe and Te atoms which tend to rotate the tetrahedra around the x axis.

The DFT calculations are in very good agreement with the measured Raman spectra, specially having in mind the strength of electronic correlations in iron based compounds and the presence of additional Fe2 atoms in the measured sample. We restricted to the nonmagnetic DFT calculations. This is because small changes in the phonon energies due to the magnetic ordering cannot be reliably captured since the DFT does not treat strong correlation and spin-fluctuations effects. Our DFT calculations for the electronic band structure agree with the results from Ref. [42]. The calculated electronic dispersions are in rather good agreement with the ARPES measurements [42], which indicates that the main effect of the interstitial Fe2 ion is to provide additional charge and shift

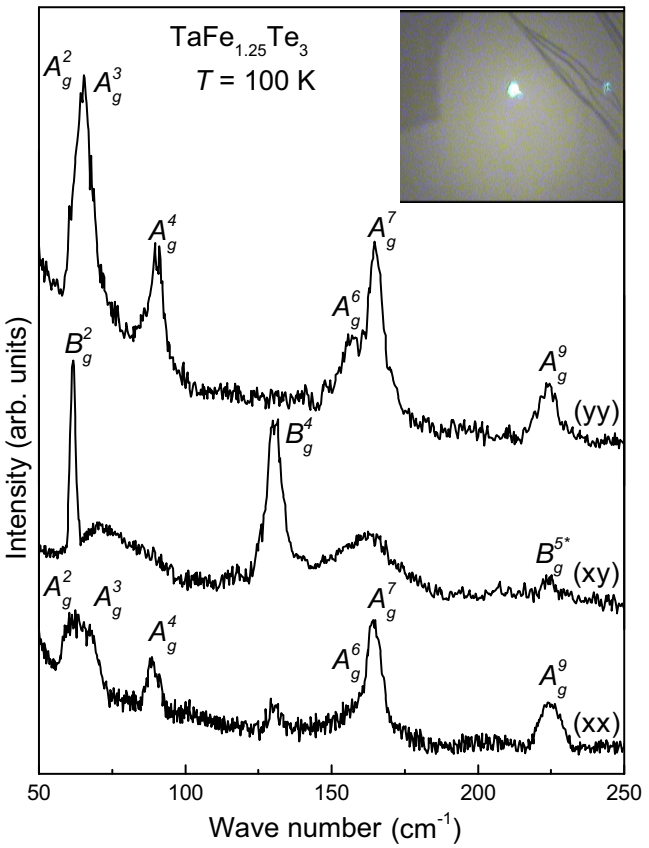

FIG. 2. Polarized Raman scattering spectra of $TaFe_{1.25}Te_3$ single crystal measured at 100 K in various polarizations. The notation in parentheses indicates the polarization directions of the incident and scattered light according to Fig. 1(a). Inset: surface of the probed $TaFe_{1.25}Te_3$ single crystal.

the Fermi level. This conclusion is supported with a small difference between the relaxed and experimental fractional coordinates; see Table I.

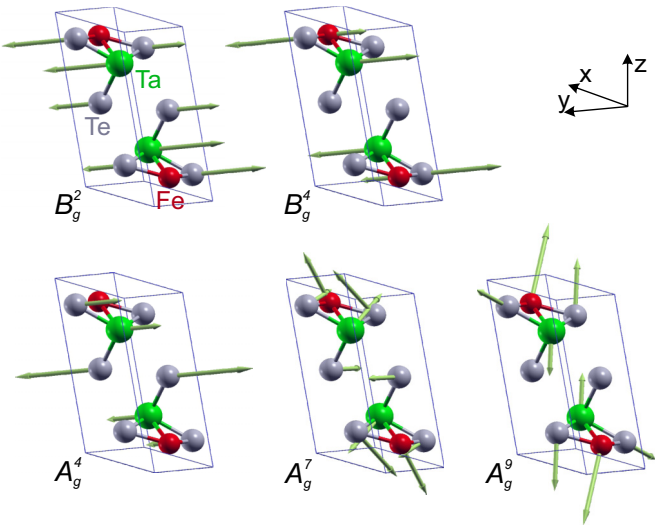

FIG. 3. Unit cell of $TaFeTe_3$ single crystal with the displacement patterns of several A_g and B_g Raman modes. Arrow lengths are proportional to the square root of the interatomic forces.

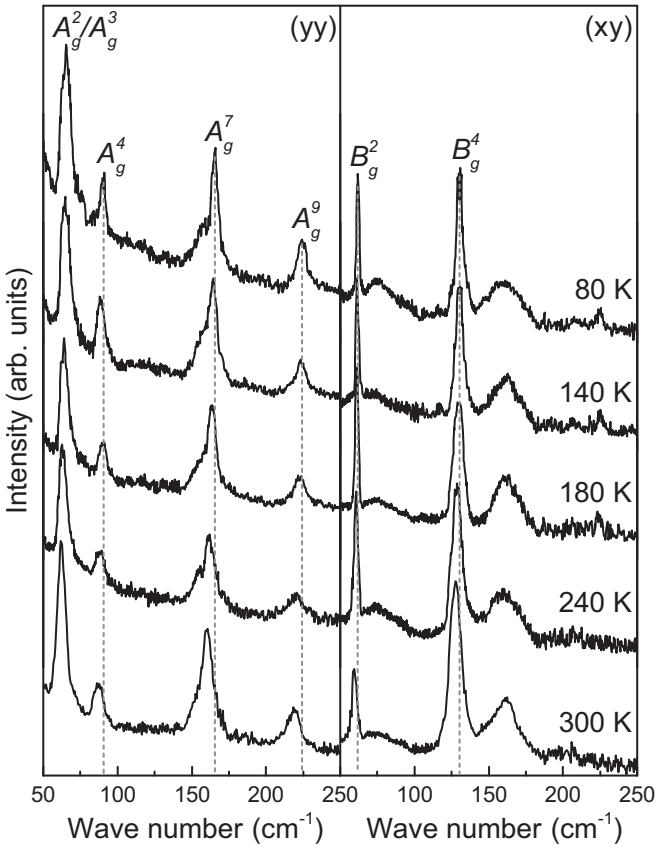

FIG. 4. Temperature dependent Raman scattering spectra of $TaFe_{1.25}Te_3$ single crystal in the (yy) (left panel) and (xy) (right panel) polarization.

In order to analyze the changes of the Raman spectra near the AFM transition at $T_N \approx 200$ K, we have performed measurements in a temperature range from 80 K up to 300 K. Raman spectra of $TaFe_{1.25}Te_3$ single crystal, measured at different temperatures in the (yy) and (xy) scattering configurations, are given in Fig. 4. In the following, we perform the temperature analysis of the energy and the linewidth for five most clearly observed modes.

The temperature dependence of the Raman mode energy is usually described with [47,48]

$$\omega_i(T) = \omega_{0,i} + \Delta_i^V(\gamma_i,\alpha_i(T)) + \Delta_i^A(C_i), \qquad (1)$$

where $\omega_{0,i}$ is a temperature independent contribution to the Raman mode energy. The second term represents a change of the phonon energy induced by the lattice thermal expansion and depends on the Grüneisen parameter γ_i and the thermal expansion coefficient $\alpha_i(T)$. The term Δ_i^A describes the anharmonicity induced change of the Raman mode energy which is a function of the anharmonic constant C_i. Both Δ_i^V and Δ_i^A have qualitatively the same temperature dependence. Since there are no reported experimental data on the temperature dependence of the lattice parameters for $TaFe_{1+y}Te_3$, we didn't attempt to fit the data, and the black dotted lines in Figs. 5 and 6 are guides to the eye. The $\omega_i(T)$ curves follow the "standard" [5,15,37,49,50] continuous decrease in energy with temperature, with very small anomalies near T_N except for the A_g^4 mode.

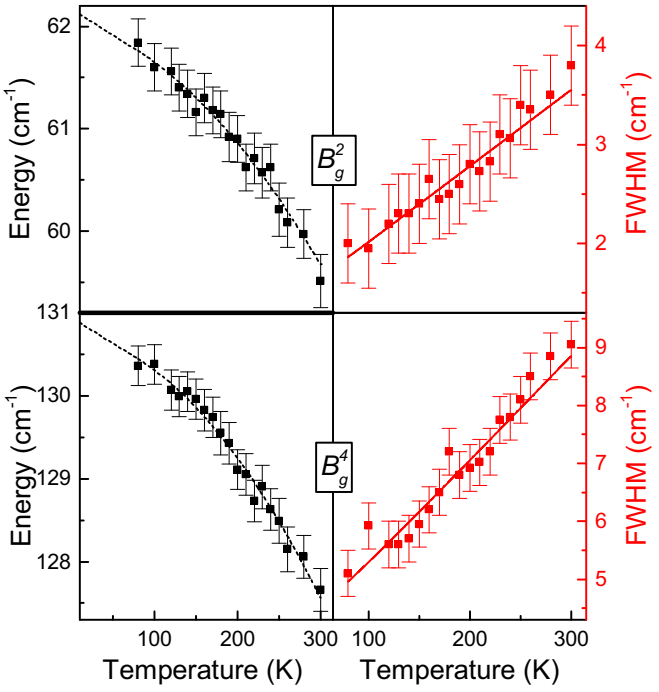

FIG. 5. Temperature dependence of the energy and linewidth for the B_g^2 and B_g^4 Raman modes of the $TaFe_{1.25}Te_3$ single crystal. The red lines are fitted according to Eq. (2), whereas black lines are guides to the eye.

The temperature dependences of the linewidth of selected B_g and A_g modes are given in the right panels of Figs. 5 and 6, respectively. While the B_g^2 and B_g^4 phonon modes do not show significant deviation from the usual behavior due to the anharmonicity effects, with gradual broadening with increasing temperature, the A_g^4, A_g^7, and A_g^9 modes exhibit moderate additional broadening above 200 K. The red lines present a fit to the standard formula for the temperature dependent linewidth due to the anharmonicity [11,47,51]:

$$\Gamma_i(T) = \Gamma_{0,i}\left(1 + \frac{2}{e^{\hbar\omega_{0,i}/2k_BT} - 1}\right) + A_i, \qquad (2)$$

where $\Gamma_{0,i}$ is the anharmonic constant and A_i is the constant term due to the disorder and electron-phonon interaction [52]. The deviation from these anharmonicity curves is most pronounced around T_N (see the insets of Fig. 6).

We can observe that all Raman modes have moderate linewidth and exhibit small anomalies near T_N. This shows that the phase transition is continuous, in agreement with the thermodynamic and transport measurements [22]. Small anomalies in the phonon spectra, which are restricted only to the vicinity of the phase transition, imply that the electron-phonon interaction of Raman active modes does not change with temperature. This is in agreement with the recent ARPES measurements which show negligible change of the Fermi surface across the AFM transition [42], indicating that the magnetic transition is not driven by the Fermi surface instability. The anomalies in the linewidth of some phonon modes near T_N are likely the signature of the increased scattering by spin fluctuations near the phase transition [51,53].

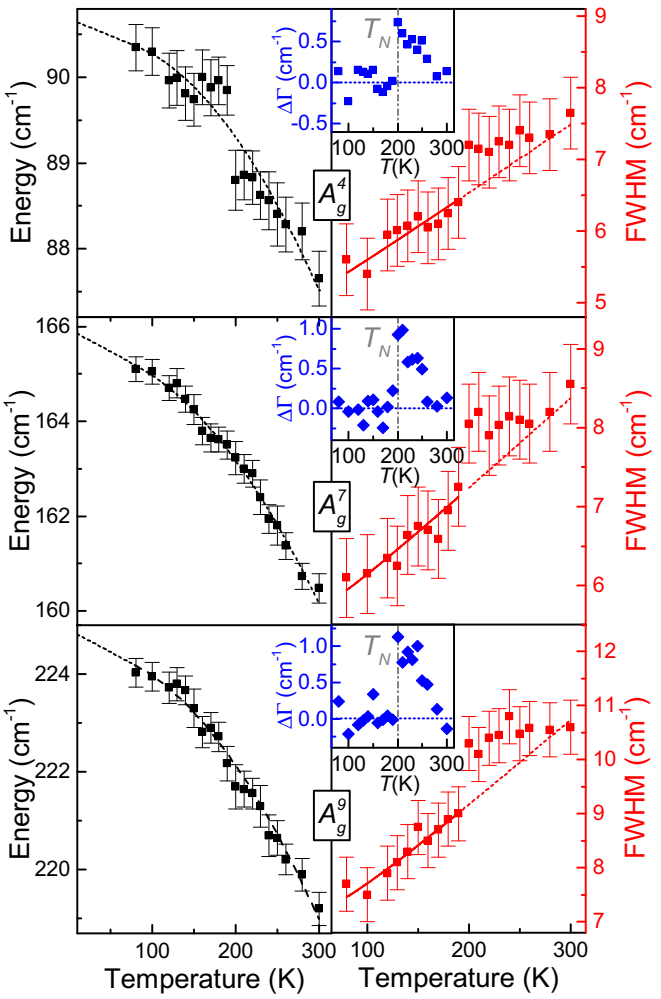

FIG. 6. Energy and linewidth of the A_g^4, A_g^7, and A_g^9 Raman modes of the $TaFe_{1.25}Te_3$ single crystal as a function of temperature. The red lines are plotted according to Eq. (2), and the black dotted lines are guides to the eye. The insets represent deviations of the Raman mode linewidth from the anharmonic form.

The density of states (DOS) at the Fermi level is not large. This can be concluded from the ARPES experiments [42] which have shown three bands crossing the Fermi level but with strong dispersion, while several relatively flat bands are found only well below the Fermi level. The DFT calculations also give moderate values for the DOS, $N(E_F) \approx 1\,\mathrm{eV}^{-1}$/f.u., after the Fermi level is shifted due to the additional charge provided by the Fe2 atoms. This value for the DOS also suggests that the electron-phonon coupling is not strong in $TaFe_{1.25}Te_3$, since it is proportional to $N(E_F)$.

$TaFe_{1.25}Te_3$ has a similar moment size as $Fe_{1+y}Te$, $\approx 2\mu_B$/Fe. However, the differences in the magnetic ordering and crystal structure cause different phonon properties of these two compounds. Namely, the phonon lines in the Raman spectra of $Fe_{1+y}Te$ have very large linewidth and pronounced anomalies both in the frequency and in the linewidth near the first order phase transition [11,13]. Small anomalies in the Raman spectra of $TaFe_{1.25}Te_3$ as compared to $Fe_{1+y}Te$ can be ascribed to the continuous, second order nature of the AFM transition and smaller electron-phonon coupling due to lower DOS at the

Fermi level. Also, the monoclinic angle β in the $TaFe_{1.25}Te_3$ unit cell significantly differs from 90° and therefore the form of the vibrational modes is different.

IV. CONCLUSION

In summary, we have performed the Raman scattering study of the zigzag spin chain $TaFe_{1.25}Te_3$ single crystal, together with the lattice dynamics calculations of $TaFeTe_3$. By analyzing the Raman spectra in different polarization configurations and using numerical calculations we have assigned nine Raman active modes predicted by the FGA. Very good agreement between the experimental frequencies and those calculated for the stoichiometric compound shows that the excess iron atoms weakly influence the phonon energies but provide momentum conservation for the phonon scattering away from Γ point. The temperature dependence of the frequency and the linewidth of the B_g Raman modes looks conventional, governed by the anharmonicity effects. While in a broad temperature range the behavior of the A_g modes is also conventional, there are clear anomalies near the AFM transition. The anomalies in the frequency and the linewidth are in the form of small kinks near T_N. This implies that the electron-phonon interaction and the DOS at the Fermi level are approximately constant in the measured temperature range. The increase in the linewidth near T_N is likely due to the coupling of spin fluctuations and vibration near the second order phase transition.

ACKNOWLEDGMENTS

We thank D. Stepanenko for useful discussions. This work was supported by the Serbian Ministry of Education, Science and Technological Development under Projects No. ON171032, No. III45018, and No. ON171017, and by the European Commission under H2020 project VI-SEEM, Grant No. 675121. Work at Brookhaven is supported by the Center for Emergent Superconductivity, an Energy Frontier Research Center funded by the U.S. DOE, Office for Basic Energy Science (C.P. and Y.M.). Numerical calculations were performed on the PARADOX supercomputing facility at the Scientific Computing Laboratory of the Institute of Physics Belgrade.

[1] Y. Kamihara, T. Watanabe, M. Hirano, and H. Hosono, J. Am. Chem. Soc. **130**, 3296 (2008).
[2] L. Ma, G. F. Ji, J. Dai, X. R. Lu, M. J. Eom, J. S. Kim, B. Normand, and W. Yu, Phys. Rev. Lett. **109**, 197002 (2012).
[3] B. Wei, H. Qing-Zhen, C. Gen-Fu, M. A. Green, W. Du-Ming, H. Jun-Bao, and Q. Yi-Ming, Chin. Phys. Lett. **28**, 086104 (2011).
[4] G. R. Stewart, Rev. Mod. Phys. **83**, 1589 (2011).
[5] M. Opačić, N. Lazarević, M. M. Radonjić, M. Šćepanović, H. Ryu, A. Wang, D. Tanasković, C. Petrovic, and Z. V. Popović, J. Phys.: Condens. Matter **28**, 485401 (2016).
[6] Z. S. Gönen, P. Fournier, V. Smolyaninova, R. Greene, F. M. Araujo-Moreira, and B. Eichhorn, Chem. Mater. **12**, 3331 (2000).
[7] H. Lei, H. Ryu, A. I. Frenkel, and C. Petrovic, Phys. Rev. B **84**, 214511 (2011).
[8] F. Han, X. Wan, B. Shen, and H.-H. Wen, Phys. Rev. B **86**, 014411 (2012).
[9] M. H. Fang, H. M. Pham, B. Qian, T. J. Liu, E. K. Vehstedt, Y. Liu, L. Spinu, and Z. Q. Mao, Phys. Rev. B **78**, 224503 (2008).
[10] S. Li, C. de la Cruz, Q. Huang, Y. Chen, J. W. Lynn, J. Hu, Y.-L. Huang, F.-C. Hsu, K.-W. Yeh, M.-K. Wu, and P. Dai, Phys. Rev. B **79**, 054503 (2009).
[11] V. Gnezdilov, Y. Pashkevich, P. Lemmens, A. Gusev, K. Lamonova, T. Shevtsova, I. Vitebskiy, O. Afanasiev, S. Gnatchenko, V. Tsurkan, J. Deisenhofer, and A. Loidl, Phys. Rev. B **83**, 245127 (2011).
[12] Y. J. Um, A. Subedi, P. Toulemonde, A. Y. Ganin, L. Boeri, M. Rahlenbeck, Y. Liu, C. T. Lin, S. J. E. Carlsson, A. Sulpice, M. J. Rosseinsky, B. Keimer, and M. Le Tacon, Phys. Rev. B **85**, 064519 (2012).
[13] Z. V. Popović, N. Lazarević, S. Bogdanović, M. M. Radonjić, D. Tanasković, R. Hu, H. Lei, and C. Petrovic, Solid State Commun. **193**, 51 (2014).
[14] K.-Y. Choi, D. Wulferding, P. Lemmens, N. Ni, S. L. Bud'ko, and P. C. Canfield, Phys. Rev. B **78**, 212503 (2008).
[15] M. Rahlenbeck, G. L. Sun, D. L. Sun, C. T. Lin, B. Keimer, and C. Ulrich, Phys. Rev. B **80**, 064509 (2009).
[16] F. Chen, M. Xu, Q. Q. Ge, Y. Zhang, Z. R. Ye, L. X. Yang, J. Jiang, B. P. Xie, R. C. Che, M. Zhang, A. F. Wang, X. H. Chen, D. W. Shen, J. P. Hu, and D. L. Feng, Phys. Rev. X **1**, 021020 (2011).
[17] W. Li, H. Ding, P. Deng, K. Chang, C. Song, K. He, L. Wang, X. Ma, J.-P. Hu, P. Chen, and Q.-K. Xue, Nat. Phys. **8**, 126 (2012).
[18] N. Lazarević, M. Abeykoon, P. W. Stephens, H. Lei, E. S. Bozin, C. Petrovic, and Z. V. Popović, Phys. Rev. B **86**, 054503 (2012).
[19] M. Badding, J. Li, F. DiSalvo, W. Zhou, and P. Edwards, J. Solid State Chem. **100**, 313 (1992).
[20] J. Neuhausen, E. Potthoff, W. Tremel, J. Ensling, P. Gütlich, and R. Kremer, Z. Naturforsch. B **48**, 797 (1993).
[21] C. Perez Vicente, M. Womes, J. C. Jumas, L. Sanchez, and J. L. Tirado, J. Phys. Chem. B **102**, 8712 (1998).
[22] R. H. Liu, M. Zhang, P. Cheng, Y. J. Yan, Z. J. Xiang, J. J. Ying, X. F. Wang, A. F. Wang, G. J. Ye, X. G. Luo, and X. H. Chen, Phys. Rev. B **84**, 184432 (2011).
[23] X. Ke, B. Qian, H. Cao, J. Hu, G. C. Wang, and Z. Q. Mao, Phys. Rev. B **85**, 214404 (2012).
[24] E. Dagotto, Rev. Mod. Phys. **85**, 849 (2013).
[25] W. Li, C. Setty, X. H. Chen, and J. Hu, Front. Phys. **9**, 465 (2014).
[26] E. Dagotto, J. Riera, and D. Scalapino, Phys. Rev. B **45**, 5744 (1992).
[27] E. Dagotto and T. M. Rice, Science **271**, 618 (1996).
[28] E. Dagotto, Rep. Prog. Phys. **62**, 1525 (1999).
[29] M. Uehara, T. Nagata, J. Akimitsu, H. Takahashi, N. Môri, and K. Kinoshita, J. Phys. Soc. Jpn. **65**, 2764 (1996).
[30] A. Hisada, K. Matsubayashi, Y. Uwatoko, N. Fujiwara, G. Deng, E. Pomjakushina, K. Conder, D. M. Radheep, R. Thiyagarajan, S. Esakkimuthu, and S. Arumugam, J. Phys. Soc. Jpn. **83**, 073703 (2014).

[31] H. Takahashi, A. Sugimoto, Y. Nambu, T. Yamauchi, Y. Hirata, T. Kawakami, M. Avdeev, K. Matsubayashi, F. Du, C. Kawashima, H. Soeda, S. Nakano, Y. Uwatoko, Y. Ueda, T. J. Sato, and K. Ohgushi, Nat. Mater. **14**, 1008 (2014).
[32] A.-M. Zhang and Q.-M. Zhang, Chin. Phys. B **22**, 087103 (2013).
[33] M. Opačić and N. Lazarević, J. Serb. Chem. Soc. **82**, 957 (2017).
[34] L. Zhang, T. Fujita, F. Chen, D. L. Feng, S. Maekawa, and M. W. Chen, Phys. Rev. B **79**, 052507 (2009).
[35] Y. Gallais, A. Sacuto, M. Cazayous, P. Cheng, L. Fang, and H. H. Wen, Phys. Rev. B **78**, 132509 (2008).
[36] V. Gnezdilov, Y. G. Pashkevich, P. Lemmens, D. Wulferding, T. Shevtsova, A. Gusev, D. Chareev, and A. Vasiliev, Phys. Rev. B **87**, 144508 (2013).
[37] A. P. Litvinchuk, B. Lv, and C. W. Chu, Phys. Rev. B **84**, 092504 (2011).
[38] K.-Y. Choi, P. Lemmens, I. Eremin, G. Zwicknagl, H. Berger, G. L. Sun, D. L. Sun, and C. T. Lin, J. Phys.: Condens. Matter **22**, 115802 (2010).
[39] S. Baroni, S. de Gironcoli, A. Dal Corso, and P. Giannozzi, Rev. Mod. Phys. **73**, 515 (2001).
[40] P. Gianozzi, S. Baroni, N. Bonini, M. Calandra, R. Car, C. Cavazzoni, D. Ceresoli, G. L. Chiarotti, M. Cococcioni, I. Dabo, A. D. Corso, S. de Gironcoli, S. Fabris, G. Fratesi, R. Gebauer, U. Gerstmann, C. Gougoussis, A. Kokalj, M. Lazzeri, L. Martin-Samos, N. Marzari, F. Mauri, R. Mazzarello, S. Paolini, A. Pasquarello, L. Paulatto, C. Sbraccia, S. Scandolo, G. Sclauzero, A. P. Seitsonen, A. Smogunov, P. Umari, and R. M. Wentzcovitch, J. Phys.: Condens. Matter **21**, 395502 (2009).
[41] D. L. Rousseau, R. P. Bauman, and S. P. S. Porto, J. Raman Spectrosc. **10**, 253 (1981).
[42] X. Min, W. Li-Min, P. Rui, G. Qing-Qin, C. Fei, Y. Zi-Rong, Z. Yan, C. Su-Di, X. Miao, L. Rong-Hua, M. Arita, K. Shimada, H. Namatame, M. Taniguchi, M. Matsunami, S. Kimura, S. Ming, C. Xian-Hui, Y. Wei-Guo, K. Wei, X. Bin-Ping, and F. Dong-Lai, Chin. Phys. Lett. **32**, 027401 (2015).
[43] R. Shuker and R. W. Gammon, Phys. Rev. Lett. **25**, 222 (1970).
[44] P. Benassi, O. Pilla, V. Mazzacurati, M. Montagna, G. Ruocco, and G. Signorelli, Phys. Rev. B **44**, 11734 (1991).
[45] H. Ryu, M. Abeykoon, K. Wang, H. Lei, N. Lazarevic, J. B. Warren, E. S. Bozin, Z. V. Popovic, and C. Petrovic, Phys. Rev. B **91**, 184503 (2015).
[46] B.-B. Zhang, N. Zhang, S.-T. Dong, Y. Lv, Y. B. Chen, S. Yao, S.-T. Zhang, Z.-B. Gu, J. Zhou, I. Guedes, D. Yu, and Y.-F. Chen, AIP Adv. **5**, 087111 (2015).
[47] J. Menéndez and M. Cardona, Phys. Rev. B **29**, 2051 (1984).
[48] H.-M. Eiter, P. Jaschke, R. Hackl, A. Bauer, M. Gangl, and C. Pfleiderer, Phys. Rev. B **90**, 024411 (2014).
[49] N. Lazarević, M. Radonjić, M. Šćepanović, H. Lei, D. Tanasković, C. Petrovic, and Z. V. Popović, Phys. Rev. B **87**, 144305 (2013).
[50] M. Opačić, N. Lazarević, M. Šćepanović, H. Ryu, H. Lei, C. Petrovic, and Z. V. Popović, J. Phys.: Condens. Matter **27**, 485701 (2015).
[51] M. N. Iliev, A. P. Litvinchuk, H.-G. Lee, C. W. Chu, A. Barry, and J. M. D. Coey, Phys. Rev. B **60**, 33 (1999).
[52] N. Lazarević, Z. V. Popović, R. Hu, and C. Petrovic, Phys. Rev. B **81**, 144302 (2010).
[53] M. N. Iliev, A. P. Litvinchuk, H.-G. Lee, C. L. Chen, M. L. Dezaneti, C. W. Chu, V. G. Ivanov, M. V. Abrashev, and V. N. Popov, Phys. Rev. B **59**, 364 (1999).